46th AIAA/ASME/ASCE/AHS/ASC Structures, Structural Dynamics & Materials Conference
18 - 21 April 2005, Austin, Texas

AIAA 2005-2301

# Thermomechanical Analysis of a Damaged Thermal Protection System

Wei H. Ng*, Peretz P. Friedmann† and Anthony M. Waas ‡
*Department of Aerospace Engineering*
*University of Michigan*
*3001 François-Xavier Bagnoud Bldg., 1320 Beal Ave.*
*Ann Arbor, Michigan 48109-2140*
Ph: (734) 763-2354 Fax: (734) 763-0578
Email: peretz@umich.edu

**Thermomechanical analysis of the space shuttle tile thermal protection system (TPS) subjected to damage is conducted using the finite element method. The thermal and structural response of the damaged configurations are compared with the undamaged configuration to determine the relative effects of damage on the thermal protection capability and the induced thermal stresses in the TPS. The TPS is modeled as a discrete three-layered structure, consisting of the LI-900 tile, strain isolation pad (SIP) and the underlying structure. The atmospheric re-entry heating profile of the Access to Space (ATS) vehicle is used for the analysis. The transient temperature distribution in the system is calculated and these results are then used to determine the thermal stresses in the system. The temperature and thermal stress solutions are assumed to be uncoupled. Three different sizes of damage having diameters 0.5", 1" and 1.5", based on hypervelocity impact, are considered. Material nonlinearity as well as cavity radiation is included in the models. The axisymmetric case is considered first and subsequently, square configurations that resemble the actual system are analyzed. The damage increases the surface area exposed to heating and affects radiation heat loss from the surface, allowing more heat to penetrate into the system. The resulting higher temperatures, coupled with stress concentrations introduced by the damage cause significant increases in the thermal stresses.**

## Nomenclature

| | |
|---|---|
| $D$ | Diameter and depth of damage in TPS |
| $E_T$ | Difference in maximum temperatures between axisymmetric and square configurations |
| $E_\sigma$ | Difference in maximum stresses between axisymmetric and square configurations |
| $q_{ATS}$ | Heat flux profile of the ATS vehicle |
| $q_1, q_2$ | Heat flux boundary conditions used in analyses |
| $r, z$ | Spatial coordinates for the axisymmetric configurations |
| $S_d$ | Tile top surface in damaged region |
| $S_u$ | Tile top surface in undamaged region |
| $t_1, t_2$ | Instances when high von Mises stresses are observed in the tile |
| $T_{axi}, T_{sq}$ | Maximum temperature for axisymmetric and square configurations, respectively |
| $x, y, z$ | Spatial coordinates for the square configurations |
| $\sigma_{Eaxi}, \sigma_{Esq}$ | von Mises stress for axisymmetric and square configurations, respectively |
| $\sigma_{axi}, \sigma_{sq}$ | Maximum von Mises stress for axisymmetric and square configuration, respectively |
| $\sigma_{ij}$ | Components of stress tensor |

* Ph.D. Candidate
† François-Xavier Bagnoud Professor, Fellow AIAA
‡ Professor, Associate Fellow, AIAA

## I. Introduction and Problem Statement

The thermal protection system (TPS) of space transportation vehicles protects the vehicle and its payload from the high temperatures generated during re-entry into the Earth's atmosphere. The TPS for reusable launch vehicles (RLV), unlike materials used previously (such as ablators in the late 1960's), have to survive multiple launches. Therefore, the TPS has to withstand not only thermal loads, but in addition, it has to survive mechanical loads as well as harsh chemical environments repeatedly without failure. Scotti, Clay and Rezin[1] provide an overview of the structural and material technologies that are currently in use and considered to be potential candidates for TPS in RLV's.

A variety of TPS have been studied analytically and experimentally. Since NASA's Space Shuttle is the first generation reusable spacecraft, it is obvious that most studies focus on this particular type of TPS. Ko and Jenkins[2] analyzed the Space Shuttle tile using a one-dimensional temperature profile across the tile's thickness. Sawyer[3] investigated the strains developed in the shuttle tile due to aerodynamic loads and substructure deformations. Experimental verifications of the shuttle tile performance were carried out by Moser and Schneider,[4] as well as Cooper et. al.[5] Operational performance of the TPS on the shuttle obtained from flight tests of the shuttle Columbia was evaluated by Ried et. al.,[6] Dotts, Smith and Tillian,[7] and Neuenschwander, Mcbride and Armour.[8] Different TPS, not used on the shuttle, have also been considered. Shideler et. al.[9] performed several analytical and experimental tests on the multiwall TPS. Milos and Squire[10] conducted a finite element (FE) analysis of the thermal protection system for the X-34 leading edge. Shideler Webb and Pittman[11] conducted verification tests on newer TPS concepts, which are less fragile than those currently used on the space shuttle. Thermal and structural FE analyses of an advanced metallic TPS were conducted by Blosser et. al.[12]

The recent accident of the NASA Shuttle Columbia highlighted the need for careful study of the effects of damage on the TPS performance. With the exception of Reference 11, where a surface-heating test on damaged TPS was conducted, almost no work has been done in this area.

The TPS of the shuttle, specifically the LI-900 high temperature reusable surface insulation tile, was selected for this study. The tiles are comprised of very high purity low-density silica, which has low coefficient of thermal expansion and small modulus of elasticity, and therefore are suitable for TPS application. The tiles are brittle, and thus require isolation from mechanical and thermal strains sustained by the underlying structure. This is the role of the strain isolation pad (SIP) located between the tile and the underlying structure. The three components, tile, SIP, and underlying structure, are attached to each other using a room-temperature galvanizing (RTV) silicone adhesive. A schematic of the combined underlying structure and TPS is shown in Figure 1.

The main objective of this paper is to determine the effects of damage on the performance and structural integrity of the TPS using finite element modeling. It is the goal of this research to complement the numerical study with experimental data, obtained from a parallel experimental effort that is currently in progress.

To achieve this objective, the thermomechanical behavior of two candidate segments of a damaged TPS are considered. First, a simple axisymmetric case is considered, and next, a square segment of a three-layered system shown in Figure 2 is examined. For each case, a transient heat flux profile is applied to the external surface of the tile and the inner surface and the sides are assumed to be insulated. It is expected that the physical insight that will be gleaned from these simulations will facilitate the tests, which will be conducted in a high temperature structural testing facility that is currently under construction.

## II. Finite Element Analysis

The finite element simulation described in this section uses the ABAQUS code version 6.4[13] to obtain the thermomechanical response of the damaged TPS. Two cases are considered: a relatively simple axisymmetric case and a square segment that resembles the actual configuration.

The axisymmetric case is based on the assumption that the system can be modeled as a circular segment with a diameter of 6" (see Figure 3). The damage profile shown in Figure 3, is based on the so-called "hypervelocity impact"[14] which produces an actual damage profile illustrated in Figure 4. The actual damage in the models is replaced by an approximate damage profile that consists of a cylindrical hole, ending with a spherical cap. The depth of the damaged portion is equal to its diameter.

The axisymmetric and square configurations for the $D = 1$" damaged system is shown in Figure 5. The same FE mesh is used in both the heat transfer and thermal stress analyses. The axisymmetric configuration

consists of 5,523 elements with 16,850 nodes while the square configuration consists of 112,230 elements with 164,401 nodes. For the axisymmetric case, the origin of the $z-r$ coordinate system is located on the axis of symmetry, as shown in Figure 5(a); while for the square case, the origin of the coordinate system is located on the centerline, as shown in Figure 5(b). Due to symmetry considerations, the square configuration can be represented by a one quarter model of the TPS.

For the axisymmetric configurations, The DCAX8 elements are used for the heat transfer problem and the CAX8 elements for the thermal stress problem. Both types of elements are eight-node biquadratic elements, shown in Figure 6(a), available in ABAQUS element library for axisymmetric analyses. In the square configurations, The DC3D10 and C3D10 elements are used for the heat transfer and thermal stress problem, respectively. These are ten-node quadratic tetrahedron elements, shown in Figure 6(b). The DCAX8 and DC3D10 elements have one degree of freedom per node, which is the temperature at the node. The CAX8 element has two degrees of freedom, $u_r$ and $u_z$, and the DC3D10 element has three degrees of freedom, $u_x$, $u_y$ and $u_z$, at each node representing the appropriate displacements for the axisymmetric and square configurations, respectively.

The presence of damage, material discontinuities, and corners give rise to stress concentrations that has to be taken into account during mesh generation, so that the mesh is sufficiently fine to capture the rapid variations in properties. It should be noted that the stress concentration associated with the damaged region is less severe than those present at the edges and corners of the material interfaces. From Figure 5, it can be seen that the mesh is refined near the damaged region, as well as the edges and corners of the material interfaces. The refinement in the mesh is introduced manually and the mesh size is limited by the maximum number of nodes and elements that can be handled by the meshing software used. The characteristic lengths of the elements range from 0.0008 m to 0.0015 m for the axisymmetric configurations and 0.001 m to 0.0045 m for the square configurations.

In the analyses, thermal-mechanical coupling, which represents the conversion of mechanical energy to thermal energy, is neglected, compared to the much larger amount energy supplied to the system via thermal loading. Thus, the thermomechanical response of the system is obtained in two independent steps. In the first step, the heat transfer problem is solved to obtain the time-dependent temperature distribution in the TPS system due to the applied thermal loads and the boundary conditions. In the second step, the thermal stresses caused by the temperature distributions are determined. The solutions are facilitated by using the same mesh for both the heat transfer and thermal stress problems.

### A. Heat Transfer Analysis

In the heat transfer analysis, the transient heat flux profile, $q_{ATS}(t)$ shown in Figure 7, applied to the top surface of the TPS, is the re-entry heat flux profile for the Access to Space (ATS) reference vehicle[15]. The sides and the inner surface of the underlying structure are assumed to be perfectly insulated, representing a worst case scenario. The TPS is characterized by the thicknesses of the three layers that comprise it as follows: LI-900 tile thickness – 3.09", SIP thickness – 0.173" and the thickness of the underlying structure is 0.063". The thickness of the tile is chosen such that the maximum temperature attained by the underlying structure is limit to 150 °C.

For the damaged configurations, there is considerable uncertainty regarding the effect of damage on the flow field and thus the heat load experienced by the TPS. To deal with this uncertainty, two thermal loading conditions, $q_1(t)$ and $q_2(t)$, which represent the lower and upper bounds of the heat load, respectively are applied. On the undamaged surface, $S_u$ in Figure 8, the ATS heat flux profile is applied. On the surface of the damage, $S_d$ in Figure 8, no heat flux is applied for the lower bound case, while the ATS heat flux profile is applied for the upper bound case, thus:

$$\text{Lower bound:} \qquad q_1(t) = \begin{cases} q_{ATS}(t) & \text{on } S_u \\ 0 & \text{on } S_d \end{cases} \tag{1}$$

$$\text{Upper bound:} \qquad q_2(t) = q_{ATS}(t) \qquad \text{on } S_u \text{ and } S_d \tag{2}$$

The primary mode of heat loss in the TPS is due to radiation from the top surface of the tile. Emissivity of the tile surface is 0.85, and is assumed to be unaffected by damage. Convection heat loss is not considered in the analysis. On the undamaged surface, all radiated heat is lost to open space. However, in

the damaged region, some of the heat radiated from the damaged surface is intercepted by opposite surfaces, as shown schematically in Figure 9, resulting in lower net heat loss to space. This cavity radiation in the damaged region is taken into account in the analysis by using the keyword commands ∗CAVITY DEFINITION and ∗RADIATION VIEWFACTOR in ABAQUS, which determines the heat exchange between element surfaces within the damage.

The densities of the LI-900 tile, SIP and underlying structure, which is made of Aluminum 2024, are 144.2 kg/m$^3$, 196.5 kg/m$^3$, and 2803 kg/m$^3$, respectively. The specific heat of the SIP is 1214.2 J/kg °C, and the thermal conductivity of the structure is 152 W/m °C. The thermal material properties that have been listed are assumed to be constant, but the specific heat and thermal conductivity of the tile, the thermal conductivity of the SIP, and the specific heat of the structure are functions of temperature. These temperature dependent properties are shown in Table 1. In the numerical computations, linear interpolation is used to determine the values at points that are in between the values of the properties listed.

The unsteady heat transfer problem is solved in the time domain by using a suitable time-step, which has to be carefully chosen so as to ensure convergence of the transient solution. This time-step is determined by repeatedly solving the heat transfer problem with decreasing time-steps. When the difference in the temperature results between two consecutive time-steps is less than 1.0 %, the solution is considered converged.

New nodal temperatures are computed at each time-step based on the time-dependent thermal loading conditions as well as the temperature distribution obtained from the previous time step. The nodal temperatures at each time step are stored for subsequent use by the thermal stress analysis.

### B. Thermal Stress Analysis

The thermal stress analysis is conducted for two types of boundary conditions, (a) the unrestrained, BC1, and (b) the restrained, BC2 boundary conditions. The schematic description of these boundary conditions is shown in Figure 10. These boundary conditions represent the upper and lower bounds for the actual boundary condition that exist in practice. The boundary conditions are applied only to the underlying structure layer since the tile and SIP are attached to the underlying structure in such a manner that they are not load bearing elements. Symmetric boundary conditions are applied to nodes lying on the axisymmetric line in the axisymmetric configurations and those lying on the planes of symmetry in the square configurations.

All mechanical material properties are assumed to be constant in the analysis and they can be found in Table 2. The displacements and stresses at each time-step are computed using the time-dependent nodal temperatures from the heat transfer solution.

## III. Results and Discussion

In this section, the damaged configurations are examined for three different levels of damage which are characterized by damage diameters, $D$ = 0.5”, 1” and 1.5”, respectively. The results of the damaged configurations are compared to the undamaged case, which is considered to be the baseline case. Furthermore, the results for the axisymmetric configurations are compared with the square configurations so as to determine the accuracy of the simple axisymmetric model.

### A. Results for the Axisymmetric Configuration

The maximum temperatures that occur in the tile, SIP and underlying structure, and the times at which they occur for the undamaged and damaged configurations are shown in Table 3. Two values are listed for each damaged configurations: one for the $q_1$ thermal loading case in the left column and the other the $q_2$ thermal loading case, in the right column. The percentage changes in the temperatures in the damaged configurations compared to the undamaged configuration are also indicated in the table.

In the tile, the maximum temperatures due to heat load $q_1$, are found to be unaffected by damage, while the maximum temperatures, due to heat load $q_2$, are found to increase with increasing damage size. For the SIP and structure, the corresponding temperatures decrease and increase with increasing damage size. It should be noted that the maximum temperatures in the SIP and structure are reached long after the vehicle has landed, as implied by the duration of 2100 seconds in Figure 7. This is a well known behavior in return from space type of structures which experience temperature “soaking” after landing. This process can cause damage in the structure.

Figure 11 depicts the contour plots of the temperature distribution, in °C, at times when the maximum von Mises stresses for the tile occur for both the restrained and unrestrained boundary conditions. The color-coded contour bands for all plots represent the same values to allow easy comparison. These figures provide a comparison of the undamaged, and the $D$ = 1" damaged configurations. The temperature contours for the $q_1$ thermal loading case are similar to the undamaged case except for changes due to the presence of damage. The temperatures associated with the damage for the $q_2$ thermal loading case are much higher, as evident in the presence of the yellow, orange and red contour bands shown in Figure 11(c).

The corresponding contour plots for the von Mises stresses in Pascal are shown in Figure 12. The von Mises stress,[16] $\sigma_E$ for the axisymmetric analysis is defined as

$$\sigma_{Eaxi} = \sqrt{\sigma_{rr}^2 + \sigma_{zz}^2 - \sigma_{zz}\sigma_{rr} + 3\sigma_{zr}^2} \tag{3}$$

This quantity is also known as the equivalent tensile stress. The von Mises theory states that a ductile material will yield when the von Mises stress reaches the material's yield stress in uniaxial tension.

All three layers of the system are shown in Figure 12. A deformation factor of 50 is applied in all figures. As the maximum stress in the structure is approximately two to three times larger than that in the tile, to ensure that the contour bands have the resolution to capture the stress distribution in the tile, stresses larger than 140 kPa are represented by the maximum band, color-coded in red, while the rest of the contour bands are equally divided to represent the stresses below 140 kPa. The locations where the maximum stresses occur for the tile are also indicated in the figures. Note that the contour plots between the restrained and unrestrained configurations for both $q_1$ and $q_2$ thermal loading cases are very similar. The principal effect of the boundary conditions is on the underlying structure, as will be shown later.

There are two time regions, denoted as $t_1$ and $t_2$ for convenience, where high von Mises stresses in the tile are observed. The precise value of $t_1$ and $t_2$ is dependent on the configuration and the level of damage. Table 4 shows the maximum von Mises stress in the tile and the times at which they occur for both thermal loading cases at $t_1$. In the table, two maximum stresses, one for the unrestrained boundary condition, BC1, and one for the restrained boundary condition, BC2, are provided. The percentage changes in these stresses in the damaged configurations, with respect to the undamaged configuration, are also indicated.

The maximum stresses in the tile are found to increase with damage for both $q_1$ and $q_2$ thermal loading cases, and the times when these stresses occur appears to be insensitive to damage size. These stresses occur approximately when the increasing surface heating rate reaches a plateau, associated with the highest heat flux, as shown in Figure 7. For the $q_1$ heating case, the maximum stresses decrease with increasing damage size. These maximum stresses occur at the upper surface of the damaged region, as shown in Figures 12(c) and (d). For the $q_2$ heating case, the maximum tile stresses occur inside the damaged region, as shown in Figures 12(d) and (e), and these stresses increase with increasing damage size.

High von Mises stresses in the tile at $t_2$ are only evident in cases with the unrestrained boundary condition. The maximum von Mises stresses for the tile at time $t_2$ are shown in Table 5. The maximum von Mises stress in the tile at $t_2$ occurs at the edge of the tile, at the tile-SIP interface which is a site of stress concentration. The maximum stresses for the SIP occur at the edge of the SIP, but depending on the configuration, either at the tile-SIP or SIP-underlying structure interface which are also regions of stress concentration. The stress concentration is due to material discontinuity and edge effects. The meshes associated with the models used in this paper do not have sufficient resolution to capture the rapid changes in stresses occurring at stress concentration regions due to material discontinuity and sharp corners. As indicated earlier in the paper, the maximum number of elements that can be used is limited by the meshing software used. Thus the stresses in these regions are not sufficiently accurate to be used for comparison purposes. The stress results in the tile at $t_2$ and in the SIP listed in Tables 5 and 6 are for selected locations that are sufficiently distant (about 0.0016 m) from the stress concentration regions and therefore can be considered accurate.

The maximum von Mises stresses and the times at which they occur for the SIP for both the restrained and unrestrained boundary conditions are shown in Table 6, while that for the underlying structure are in Table 7. Damage decreases the maximum stresses in the SIP as well as in the underlying structure for the lower bound thermal loading case, $q_1$, but increases the maximum stresses for the upper bound thermal loading case, $q_2$.

**B. Square Configuration**

The maximum temperatures that occur in the tile, SIP and underlying structure, and the times at which they occur for the undamaged and damaged configurations are shown in Table 8. The general trend of the temperatures with respect to damage size is similar to that observed in the axisymmetric configurations; temperatures are found to decrease with increasing damage size for the $q_1$ loading case and they increase with increasing damage size for the $q_2$ loading case. The lower bound maximum temperatures in the tile occur outside of the damaged area and are not affected by cavity radiation, thus these temperatures are insensitive to damage. The upper bound maximum temperatures for the tile, which occur within the damaged area of the tile, increased significantly. For the square configuration, the $D$ = 1.5" damage increases the temperature by 54.4 % to 1515 °C, which is below the tile's melting temperature of 1700 °C, but above its softening temperature of 1370 °C.

For the SIP and underlying structure, the lower bound temperatures are found to decrease with increasing damage size. However, the upper bound maximum temperatures for these layers increase with increasing damage size. Since no heat flux is applied to the damaged surface for the $q_1$ case, the presence of damage reduces the surface area subjected to heating. Therefore, the total heating rate is reduced, resulting in lower amount of energy supplied to the TPS. For the $q_2$ case, the presence of damage increases the surface area subjected to the thermal loading, at the same time allowing the heat load to penetrate deeper into the system resulting in higher temperatures. For the $D$ = 1.5" damaged configuration, the temperature in the structure is found to increase by 49.3%.

Contour plots of the temperature, in °C, and the von Mises stress, in Pascal, similar to those presented in the previous section, are shown in Figures 13 and 14, respectively. The von Mises stress in the square configuration is defined as

$$\sigma_{Esq} = \sqrt{\sigma_{xx}^2 + \sigma_{yy}^2 + \sigma_{zz}^2 - \sigma_{xx}\sigma_{yy} - \sigma_{yy}\sigma_{zz} - \sigma_{zz}\sigma_{xx} + 3\sigma_{xy}^2 + 3\sigma_{yz}^2 + 3\sigma_{zx}^2} \tag{4}$$

As noted for the axisymmetric case, the contour plots between the restrained and unrestrained cases are similar. Thus only the unrestrained configurations are shown in Figure 14. Note the similarities in the contour features between the axisymmetric and square configurations close to the damaged region. These similarities diminish as one moves away from the damaged region towards the edge.

The maximum von Mises stresses for the tile at $t_1$ are shown in Table 9. In the $q_1$ case, the highest temperature associated with the damaged region is found on the upper surface of the damage. Even though the temperature is approximately equal to that in the undamaged configuration, the stress increases due to the stress concentration of the damage. Unlike the stress concentrations caused by material discontinuities and sharp corners, the stress concentration in the damaged region is mild and can be adequately resolved by the mesh. In the $q_2$ case, the maximum temperature occurs within the damaged region. The higher temperatures, coupled with the stress concentration introduced by the damage, increase the stresses significantly. For the axisymmetric configuration, the maximum stress in the tile at $t_1$ for the $q_2$ thermal loading case increases with respect to damage size, but for the square configuration, the maximum stress for the $D$ = 0.5" damaged configuration is larger than that for the $D$ = 1" damaged configuration, even though temperatures are higher in the $D$ = 1" damaged configuration.

The maximum tile stresses that occur at $t_2$ are given in Table 10 and the maximum von Mises stresses in the SIP and underlying structure are shown in Tables 11 and 12, respectively. As evident, the maximum values occur approximately at the time when the SIP and structure reach their maximum temperature, and they are caused predominantly by the mismatch in the coefficients of thermal expansion between the layers. These maximum stresses are dependent on the maximum temperatures reached by the SIP and structure, and thus on the total heat applied to the system. Increasing damage decreases these stresses for the $q_1$ loading case and increases that for the $q_2$ loading case. These high stresses do not show up in the tile and SIP of the restrained case, because the boundary condition prevents the structure layer from expanding, thus reduces the effect of mismatch in the coefficients of thermal expansion. This restriction in thermal expansion of the underlying structure in the restrained case also causes much higher stresses in the underlying structure than those in the unrestrained case.

Again, the stresses in the tile at $t_2$ and SIP stresses occur at stress concentrations at corners of the material interfaces. These stresses, like those in the axisymmetric configuration, are selected from locations that are sufficiently distant (about 0.002 m) from the stress concentration regions.

### C. Comparison of Results Between the Axisymmetric and Square Configurations

The differences in maximum temperature and stress results between the axisymmetric and square configurations are shown in Figures 15 to 18. The percentage difference in maximum temperatures and stresses, $E_T$ and $E_\sigma$, respectively are defined as

$$E_T = \frac{T_{axi} - T_{sq}}{T_{sq}} \times 100\% \tag{5}$$

$$E_\sigma = \frac{\sigma_{axi} - \sigma_{sq}}{\sigma_{sq}} \times 100\% \tag{6}$$

where $T_{axi}$ and $T_{sq}$ are the maximum temperatures for the axisymmetric and square configurations, respectively, and $\sigma_{axi}$ and $\sigma_{sq}$ are the maximum von Mises stress for the axisymmetric and square configurations, respectively.

The maximum temperatures in the tile for both axisymmetric and square configurations are very similar. The simplification due to the axisymmetric case is equivalent to removing material from the corners of the square configuration and modifying the boundary conditions accordingly. The maximum temperatures in the tile occur on the undamaged tile surface or the surface within the damaged region. Since the axisymmetric simplification does not change the surface properties and damage geometry, the differences between the maximum tile temperatures of the two analyses are small, less than 0.35%.

The difference in temperature results between the axisymmetric and square configurations for the SIP and structure layers are more significant. The sizes and geometry of the damaged region are the same in both configurations, so the changes in energy supplied to the TPS due to the damage are the same. The reduction in mass for the axisymmetric configurations allows the SIP and structure to have a larger change in temperatures for the same amount of heat input to or loss from the system. Thus, the changes in maximum temperatures in the SIP and structure due to damage are higher in the axisymmetric configurations than in the square configuration.

The differences in maximum stresses in the tile at $t_1$ are relatively small, up to about 11 %. As these stresses occur in the damaged region that is distant from the edges, it is relatively insensitive to the simplifying assumptions associated with the axisymmetric configurations. For the square configurations, the maximum SIP stresses and tile stresses at $t_2$, occur at the corners of the square system at the material interfaces, which are not modeled by the axisymmetric case. Thus, the stresses in the tile at $t_2$ and the SIP selected for comparison in the axisymmetric and square configurations are from different locations. The stress concentrations in the square configuration are also more substantial than the axisymmetric case, thus differences in these stresses are larger.

Like for the SIP, the maximum stresses for the unrestrained structure in the square configuration also occur at the corners, but not at the material interface. The differences in the maximum stresses are thus large. The restrained boundary condition results in very high stresses with little variation in the underlying structure. Thus, even though the locations of structure's maximum stresses for the restrained axisymmetric and square cases are different, the small variation in the stress results produces smaller differences. Note that these differences are approximately of the same magnitude as those for temperatures in the structure.

For the maximum temperature results, the axisymmetric configurations produce relatively good results for the damage sizes considered, with differences less than 9 %. For the stress results, the differences can be as high as 57 %, because these stresses in the square configurations occur in regions that are not modeled by the axisymmetric configurations. It should be noted however, that the square configurations require approximately 15 times more degrees of freedom when compared to the axisymmetric cases, therefore the approximate axisymmetric models can be useful for rapid trend type studies where accuracy is less important than computational turn around time.

## IV. Concluding Remarks

Finite element analyses for axisymmetric and square TPS configurations were conducted to determine the effects of damage on the performance and structural integrity of a TPS. Only effects due to thermal stresses are considered and material mechanical property degradation and other effects due to failure mechanisms such as cracks formation and delamination are not considered. Damage changes the surface geometry of the tile and it modifies the radiation heat loss from the surface of the tile. A damage represented by an approximate model characterized by $D$ = 1.5" can increase the maximum temperature in

the tile by 55%. The higher temperatures in the tile also result in more heat penetrating into the inner layers, elevating the thermal stresses within the system. Stresses in the tile also increase due to the introduction of stress concentration by the damage. For the limited number of cases considered, the increase in temperatures and stresses were not sufficient to cause structural failure. However, further studies using the model are in progress. The approximate axisymmetric configuration proved itself to be useful for predicting the maximum increases in temperature due to damage; however, it produced substantial differences in the prediction of the thermal stress. On the other hand, the axisymmetric model results in large reductions in computational requirements which may be useful for preliminary design type calculations. Current ongoing research is aimed at obtaining experimental data to validate the numerical results presented in this study.

## Acknowledgements

This work was supported by the Space Vehicle Technology Institute under grant NCC3-989 jointly funded by NASA and DOD within the NASA Constellation University Institutes Project, with Claudia Meyer as the project manager.

## References

1 Scotti, S.J., Clay, C. and Rezin, M., "Structures and Materials Technologies for Extreme Environments Applied to Reusable Launch Vehicles". *AIAA/ICAS International Symposium and Exposition*, AIAA Paper 2003-2697, Dayton, OH, Jul. 2003.

2 Ko, W.L. and Jenkins, J.M., "Thermal Stress Analysis of Space Shuttle Orbiter Wing Skin Panel and Thermal Protection System", NASA Technical Memorandum 88276.

3 Sawyer, J.W., "Effect of Strain Isolator Pad on Inplane Strain in Shuttle Orbiter Thermal Protection System Tiles", NASA Technical Paper 2141.

4 Moser, T.L. and Schineider, W.C., "Strength Integrity of the Space Shuttle Orbiter Tiles", *AIAA-81-2469, 1st Flight Testing Conference,* Las Vegas, NV, NOV. 1981.

5 Cooper, P.A., Miserentino, R., Sawyer, J.W. and Leatherwood, J.D., "Effect of Simulated Mission Loads on Orbiter Thermal Protection System Undensified Tiles", *Journal of Spacecraft and Rockets*, Vol. 21, No. 5. Sep-Oct 1984

6 Ried, T.C., Goodrich, W.D., Li, C.P., Scott, C.D., Derry, S.M. and Maraia, R.J., "Space Shuttle Orbiter Entry Heating and TPS Response: STS-1 Predictions and Flight Data", *NASA Conference Publication 2216*, Pg. 327-347, 1982

7 Dotts, R.L., Smith, J.A. and Tillian, D.J., "Space Shuttle Orbiter Reusable Surface Insulation Flight Results", *NASA Conference Publication 2283, Part 2*, Pg. 949-966, 1983.

8 Neuenschwander, W.E., McBride, D.U. and Armour, G.A., "Shuttle TPS Thermal Performance and Analysis Methodology", *NASA Conference Publication 2283, Part 2*, Pg. 1025-1064, 1983.

9 Shideler, J.L., Kelly, H.N., Avery, D.E., Blosser, M.L. and Adelman, H.M., "Multiwall TPS – An Emerging Concept", *Journal of Spacecraft and Rockets*, Vol. 19, No. 4, Jul-Aug 1982.

10 Frank S. Milos and Thomas H. Squire, "Thermostructural Analysis of X-34 Wing Leading-Edge Tile Thermal Protection System", *Journal of Spacecraft and Rockets*, Vol. 36, No. 2, Mar-Apr 1999.

11 Shideler, J.L., Webb, G.L. and Pittman, C.M., "Verification Tests of Durable Thermal Protection System Concepts", *Journal of Spacecraft and Rockets*, Vol. 22, No. 6, Nov-Dec 1985.

12 Blosser, M.L., Chen, R.R., Schmidt, I.H., Dorsey, J.T., Poteet, C.C. and Bird, R.K., "Advanced Metallic Thermal Protection System Development", *AIAA 40th Aerospace Sciences Meeting & Exhibit*, AIAA Paper 2002-0504, Reno, NV, Jan. 2002

13 "ABAQUS/Standard User's Manual Version 6.4", Hibbitt, Karlsson & Sorensen, Inc., Pawtucket, RI.

14 Christiansen, E.L. and Friesen, L., "Penetration Equations for Thermal Protection Material", *International Journal Impact Engineering*, Vol. 20, Pg. 153-164, 1997

15 Myers, D.E., Martin, C.J. and Blosser, M.L., "Parametric Weight Comparison of Advanced Metallic, Ceramic Tile, and Ceramic Blanket Thermal Protection Systems", *NASA/TM-2000-210289*, June 2000

16 Barber, J.R., "Elasticity", Kluwer Academic Publishers, 2002, page 11

| T (°C) | A | B | C | D |
|---|---|---|---|---|
| -17.6 | 628.0 | 0.03165 | 0.03271 | 816.4 |
| 93.5 | – | – | – | 904.3 |
| 121.3 | 879.2 | 0.03894 | – | |
| 149.1 | – | – | – | 937.8 |
| 204.6 | – | – | 0.04636 | 975.5 |
| 260.2 | 1055 | 0.04779 | – | – |
| 315.7 | – | – | 0.06604 | – |
| 399.1 | 1151 | 0.05626 | – | – |
| 538.0 | 1206 | 0.06791 | – | – |
| 676.9 | 1239 | 0.08536 | – | – |
| 815.7 | 1256 | 0.1065 | – | – |
| 926.9 | 1264 | – | – | – |
| 954.6 | 1269 | 0.1327 | – | – |
| 1093.5 | – | 0.1632 | – | – |
| 1260.2 | – | 0.2006 | – | – |

**A** = Specific heat of LI-900 (J / kg ºC)
**B** = Conductivity of LI-900 (W / m ºC)
**C** = Conductivity of SIP (W / m ºC)
**D** = Specific heat of Aluminum 2024 (J / kg ºC)

Table 1: Temperature dependent thermal properties of the tile, SIP and underlying structure

| Material | Property | Value |
|---|---|---|
| **LI-900** | Young's modulus | 172 MPa |
| | Poisson's ratio | 0.16 |
| | Coefficient of thermal expansion | 606 nε / ºC |
| | Tensile failure strength | 165 kPa |
| **SIP** | Young's modulus | 807 kPa |
| | Poisson's ratio | 0.3 |
| | Coefficient of thermal expansion | 18 με / ºC |
| **Aluminum 2024** | Young's modulus | 72.4 GPa |
| | Poisson's ratio | 0.33 |
| | Coefficient of thermal expansion | 20.2 με / ºC |
| | Tensile failure strength | 455 MPa |

Table 2. Mechanical properties of the tile, SIP and underlying structure

| TPS Element | *D* (inch) | Temperature (°C) | | % change | | Time (s) | |
|---|---|---|---|---|---|---|---|
| Tile | 0 | 981 | | NA | | 850 | |
| | 0.5 | 981 | 1462 | 0 | 49.0 | 850 | 850 |
| | 1.0 | 981 | 1501 | 0 | 53.0 | 850 | 850 |
| | 1.5 | 981 | 1516 | 0 | 54.5 | 850 | 850 |
| SIP | 0 | 150 | | NA | | 6600 | |
| | 0.5 | 148 | 158 | -1.3 | 5.3 | 6600 | 6550 |
| | 1.0 | 143 | 188 | -4.7 | 25.3 | 6450 | 6250 |
| | 1.5 | 136 | 245 | -9.3 | 63.3 | 6200 | 5600 |
| Underlying structure | 0 | 150 | | NA | | 7150 | |
| | 0.5 | 148 | 158 | -1.3 | 5.3 | 7150 | 7100 |
| | 1.0 | 142 | 187 | -5.3 | 24.7 | 7050 | 6800 |
| | 1.5 | 135 | 244 | -10.0 | 62.7 | 6850 | 6100 |

Table 3. Maximum temperatures and times at which they occur in tile, SIP and underlying structure in axisymmetric configurations

| Thermal Loading | *D* (inch) | Max. von Mises stress (kPa) | | % change | | Time (s) | |
|---|---|---|---|---|---|---|---|
| | | BC1 | BC2 | BC1 | BC2 | BC1 | BC2 |
| $q_1$ | 0 | 61.9 | 62.0 | NA | NA | 350 | 350 |
| | 0.5 | 107.0 | 107.1 | 72.9 | 72.7 | 350 | 350 |
| | 1.0 | 94.7 | 94.8 | 53.0 | 52.9 | 350 | 350 |
| | 1.5 | 86.4 | 86.5 | 39.6 | 39.5 | 350 | 350 |
| $q_2$ | 0 | 61.9 | 62.0 | NA | NA | 350 | 350 |
| | 0.5 | 133.4 | 133.6 | 115.5 | 115.5 | 400 | 400 |
| | 1.0 | 136.5 | 136.7 | 120.5 | 120.5 | 400 | 400 |
| | 1.5 | 152.0 | 152.1 | 145.6 | 145.3 | 400 | 400 |

Table 4. Maximum von Mises stresses and times at which they occur in tile for the axisymmetric case at $t_1$ for the two different thermal loading conditions

| Thermal Loading | *D* (inch) | Max. von Mises stress (kPa) | % change | Time (s) |
|---|---|---|---|---|
| $q_1$ | 0 | 47.0 | NA | 7050 |
| | 0.5 | 46.9 | -0.2 | 7050 |
| | 1.0 | 44.9 | -4.5 | 7000 |
| | 1.5 | 42.1 | -10.4 | 6750 |
| $q_2$ | 0 | 47.0 | NA | 7050 |
| | 0.5 | 50.6 | 7.7 | 7050 |
| | 1.0 | 61.5 | 30.9 | 6700 |
| | 1.5 | 82.2 | 74.9 | 6000 |

Table 5. Maximum von Mises stress and times at which they occur in tile for the axisymmetric case at $t_2$ for the two different thermal loading conditions

| Thermal Loading | *D* (inch) | Max. von Mises stress (kPa) | | % change | | Time (s) | |
|---|---|---|---|---|---|---|---|
| | | BC1 | BC2 | BC1 | BC2 | BC1 | BC2 |
| $q_1$ | 0 | 22.0 | 4.04 | NA | NA | 7200 | 6750 |
| | 0.5 | 21.6 | 3.97 | -1.8 | -1.7 | 7150 | 6750 |
| | 1.0 | 20.7 | 3.80 | -5.9 | -5.9 | 7050 | 6650 |
| | 1.5 | 19.4 | 3.56 | -11.8 | -11.9 | 6800 | 6400 |
| $q_2$ | 0 | 22.0 | 4.04 | NA | NA | 7200 | 6750 |
| | 0.5 | 23.3 | 4.28 | 5.9 | 5.9 | 7100 | 6700 |
| | 1.0 | 28.4 | 5.20 | 29.1 | 28.7 | 6800 | 6400 |
| | 1.5 | 38.0 | 6.95 | 72.7 | 72.0 | 6050 | 5700 |

Table 6. Maximum von Mises stress and times at which they occur in the SIP for the axisymmetric case for the two different thermal loading conditions

| Thermal Loading | *D* (inch) | Max. von Mises stress (MPa) | | % change | | Time (s) | |
|---|---|---|---|---|---|---|---|
| | | BC1 | BC2 | BC1 | BC2 | BC1 | BC2 |
| $q_1$ | 0 | 1.05 | 281.2 | NA | NA | 7350 | 7150 |
| | 0.5 | 1.04 | 277.0 | -1.0 | -1.5 | 7350 | 7150 |
| | 1.0 | 0.99 | 265.1 | -5.7 | -5.7 | 7350 | 7050 |
| | 1.5 | 0.93 | 248.5 | -11.4 | -11.6 | 7100 | 6850 |
| $q_2$ | 0 | 1.05 | 281.2 | NA | NA | 7350 | 7150 |
| | 0.5 | 1.12 | 298.5 | 6.7 | 6.2 | 7300 | 7100 |
| | 1.0 | 1.36 | 363.1 | 29.5 | 29.1 | 7000 | 6800 |
| | 1.5 | 1.82 | 486.0 | 73.3 | 72.8 | 6300 | 6100 |

Table 7. Maximum von Mises stress and times at which they occur in underlying structure for the axisymmetric case for the two different thermal loading conditions

| TPS Element | *D* (inch) | Temperature (°C) | | % change | | Time (s) | |
|---|---|---|---|---|---|---|---|
| Tile | 0 | 981 | | NA | | 850 | |
| | 0.5 | 981 | 1457 | 0 | 48.5 | 850 | 850 |
| | 1.0 | 981 | 1499 | 0 | 52.8 | 850 | 850 |
| | 1.5 | 981 | 1515 | 0 | 54.4 | 850 | 850 |
| SIP | 0 | 150 | | NA | | 6600 | |
| | 0.5 | 149 | 156 | -0.7 | 4.0 | 6550 | 6550 |
| | 1.0 | 145 | 180 | -3.3 | 20.0 | 6450 | 6300 |
| | 1.5 | 139 | 225 | -7.3 | 50.0 | 6250 | 5800 |
| Underlying structure | 0 | 150 | | NA | | 7150 | |
| | 0.5 | 148 | 156 | -1.3 | 4.0 | 7150 | 7100 |
| | 1.0 | 144 | 179 | -4.0 | 19.3 | 7100 | 6850 |
| | 1.5 | 138 | 224 | -8.0 | 49.3 | 6900 | 6300 |

Table 8. Maximum temperatures and times at which they occur in the tile, SIP and underlying structure in square configurations

| Thermal Loading | *D* (inch) | Max. von Mises stress (kPa) | | % change | | Time (s) | |
|---|---|---|---|---|---|---|---|
| | | BC1 | BC2 | BC1 | BC2 | BC1 | BC2 |
| $q_1$ | 0 | 63.4 | 63.6 | NA | NA | 350 | 350 |
| | 0.5 | 111.2 | 111.6 | 75.4 | 75.5 | 350 | 350 |
| | 1.0 | 99.5 | 99.9 | 56.9 | 57.1 | 400 | 400 |
| | 1.5 | 96.4 | 96.8 | 52.1 | 52.2 | 400 | 400 |
| $q_2$ | 0 | 63.4 | 63.6 | NA | NA | 350 | 350 |
| | 0.5 | 138.1 | 138.3 | 117.8 | 117.5 | 400 | 400 |
| | 1.0 | 136.8 | 137.1 | 115.8 | 115.6 | 400 | 400 |
| | 1.5 | 149.9 | 150.0 | 136.4 | 135.8 | 400 | 400 |

Table 9. Maximum von Mises stresses and times at which they occur in tile for the square configurations at $t_1$ for the two different thermal loading conditions

| Thermal Loading | *D* (inch) | Max. von Mises stress (kPa) | % change | Time (s) |
|---|---|---|---|---|
| $q_1$ | 0 | 75.0 | NA | 7100 |
| | 0.5 | 71.3 | -4.9 | 7100 |
| | 1.0 | 68.9 | -8.1 | 7050 |
| | 1.5 | 65.5 | -12.7 | 6850 |
| $q_2$ | 0 | 75.0 | NA | 7100 |
| | 0.5 | 75.6 | 0.8 | 7100 |
| | 1.0 | 88.6 | 18.1 | 6750 |
| | 1.5 | 113.5 | 51.3 | 6250 |

Table 10. Maximum von Mises stresses and times at which they occur in tile for the square configurations at $t_2$ for the two different thermal loading conditions

| Thermal Loading | *D* (inch) | Max. von Mises stress (kPa) | | % change | | Time (s) | |
|---|---|---|---|---|---|---|---|
| | | BC1 | BC2 | BC1 | BC2 | BC1 | BC2 |
| $q_1$ | 0 | 30.1 | 4.61 | NA | NA | 7150 | 6050 |
| | 0.5 | 30.0 | 4.31 | -0.3 | -6.5 | 7250 | 5600 |
| | 1.0 | 29.0 | 4.20 | -3.7 | -8.9 | 7200 | 5450 |
| | 1.5 | 27.6 | 3.94 | -8.3 | -14.5 | 7000 | 5150 |
| $q_2$ | 0 | 30.1 | 4.61 | NA | NA | 7150 | 6050 |
| | 0.5 | 31.8 | 4.65 | 5.6 | 0.9 | 7200 | 5900 |
| | 1.0 | 37.3 | 5.45 | 23.9 | 18.2 | 6800 | 5700 |
| | 1.5 | 47.7 | 6.99 | 58.5 | 51.6 | 6350 | 5250 |

Table 11. Maximum von Mises stresses and times at which they occur in SIP for the square configurations for the two different thermal loading conditions

.

| Thermal Loading | *D* (inch) | Max. von Mises stress (MPa) | | % change | | Time (s) | |
|---|---|---|---|---|---|---|---|
| | | BC1 | BC2 | BC1 | BC2 | BC1 | BC2 |
| $q_1$ | 0 | 2.32 | 283.1 | NA | NA | 7300 | 7150 |
| | 0.5 | 2.34 | 277.9 | 0.8 | -1.8 | 7300 | 7150 |
| | 1.0 | 2.26 | 268.6 | -2.6 | -5.1 | 7250 | 7100 |
| | 1.5 | 2.16 | 255.5 | -6.9 | -9.7 | 7100 | 6900 |
| $q_2$ | 0 | 2.32 | 283.1 | NA | NA | 7300 | 7150 |
| | 0.5 | 2.48 | 294.6 | 6.9 | 4.1 | 7300 | 7100 |
| | 1.0 | 2.91 | 345.5 | 25.4 | 22.0 | 6900 | 6850 |
| | 1.5 | 3.73 | 442.3 | 60.8 | 56.2 | 6450 | 6300 |

Table 12. Maximum von Mises stresses and times at which they occur in underlying structure for the square configurations for the two different thermal loading conditions

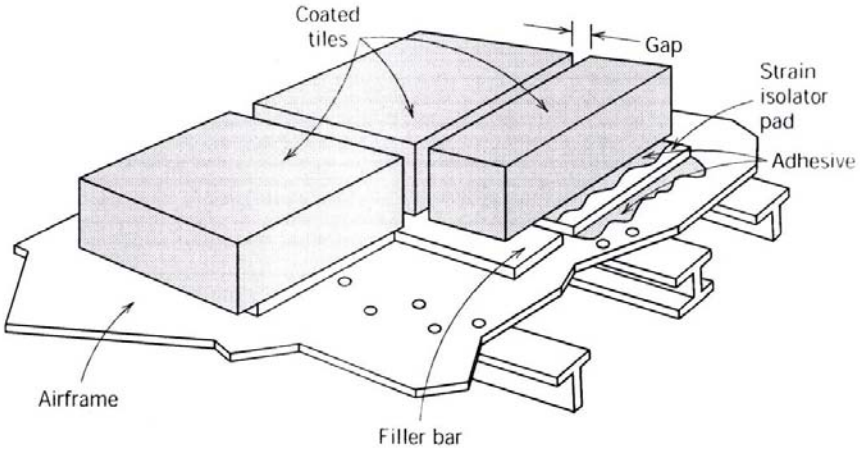


Figure 1. Space Shuttle TPS and Airframe (from Callister, W.D., "Materials Science and Engineering: An Introduction", John Wiley and Sons Inc., New York, 2003, Pg. S-349)

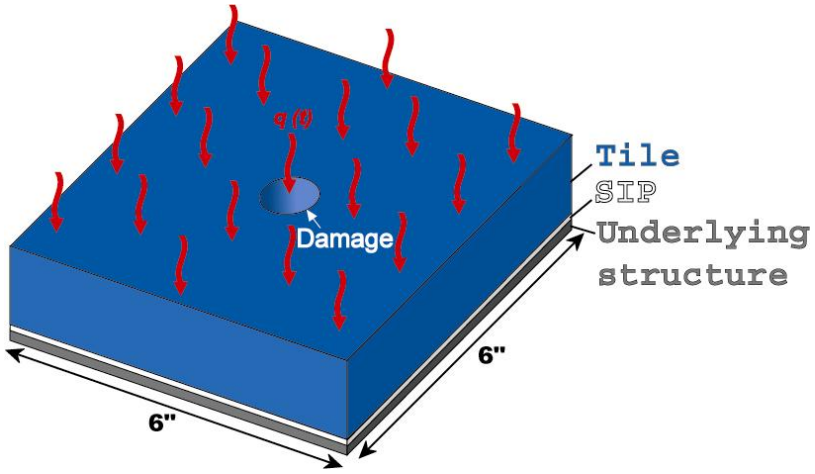


Figure 2. Schematic view of square segment of the three-layered TPS configuration

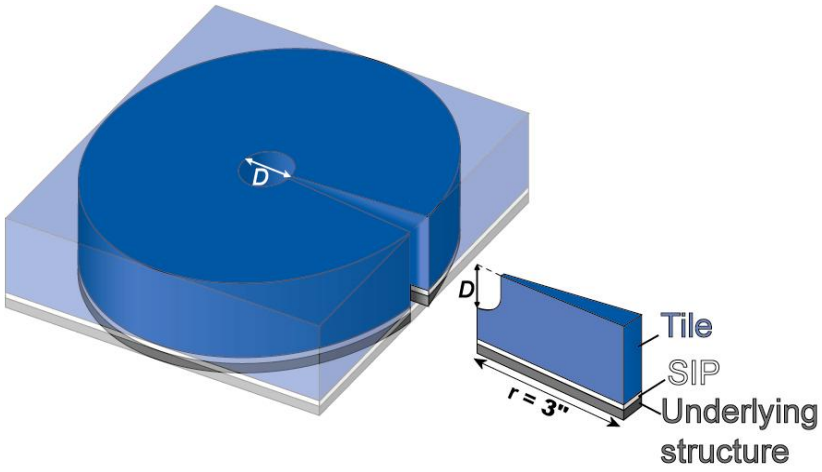


Figure 3. Circular axisymmetric configuration

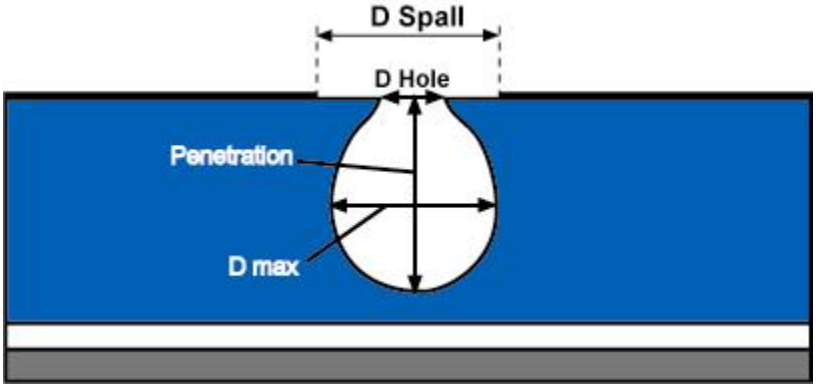


Figure 4. Damage geometry associated with hypervelocity impact.

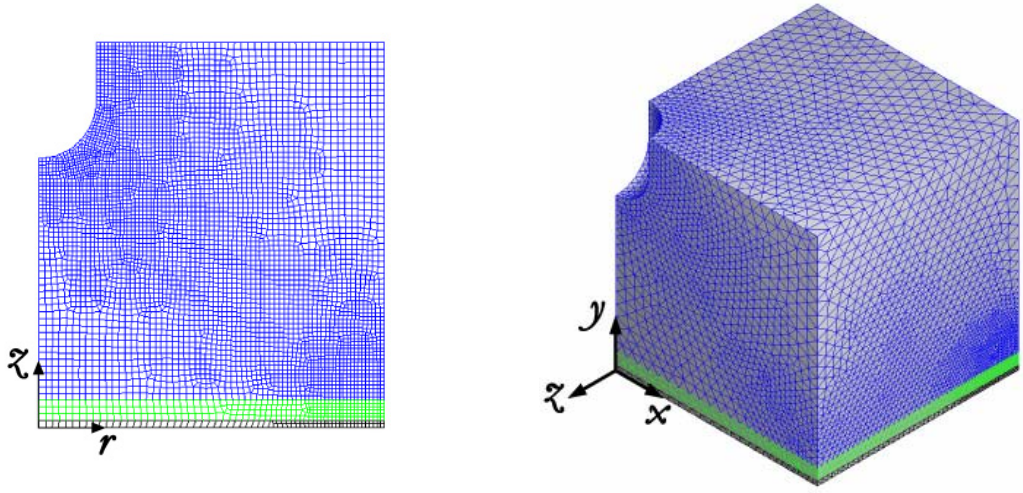


(a) (b)

Figure 5. Schematic representation of axisymmetric and square configuration illustrating damage geometry and coordinate systems

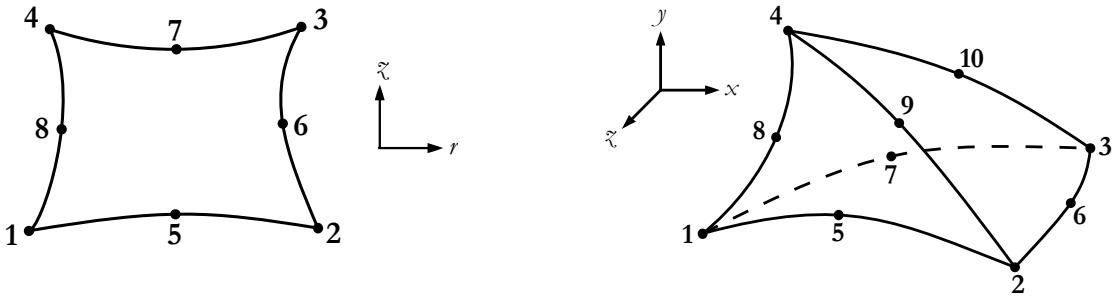


(a) 8-node biquadratic element used for axisymmetric configuration

(b) 10 node quadratic tetrahedron element used for square configuration

Figure 6. Elements used for axisymmetric and square configurations

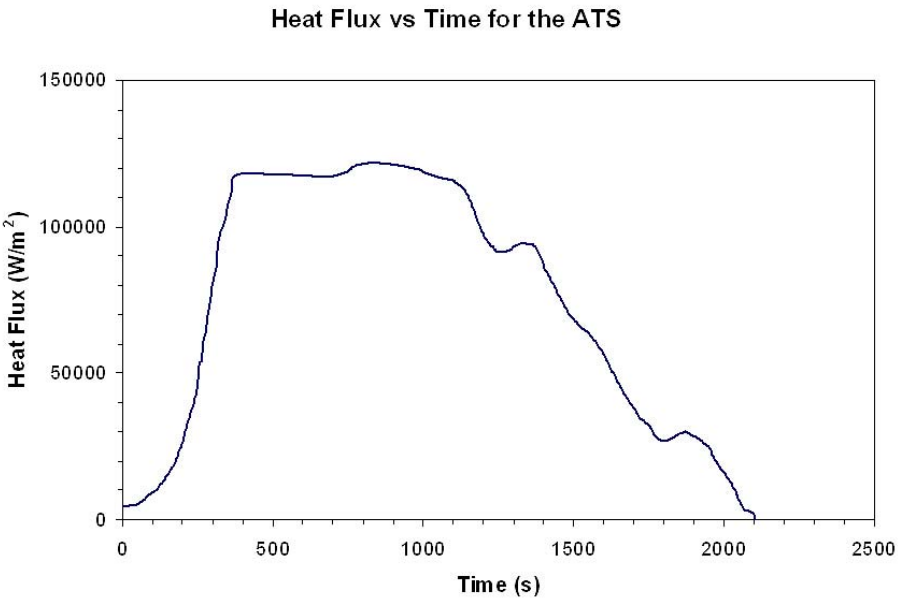


Figure 7. Re-entry heat flux loading profile for the ATS vehicle, $q_{ATS}$

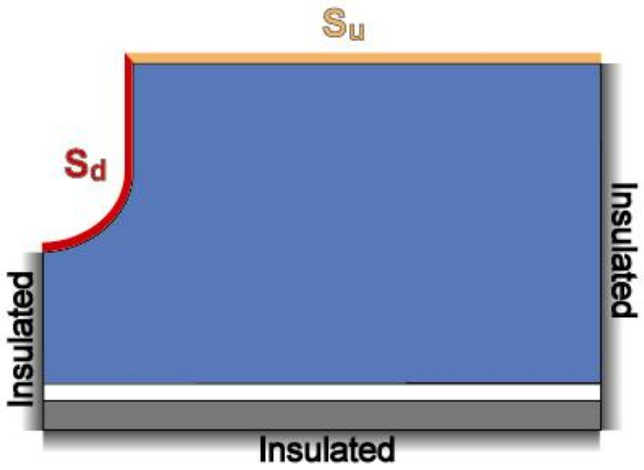


Figure 8. Cross section of TPS showing the undamaged and damaged surfaces subjected to thermal loading

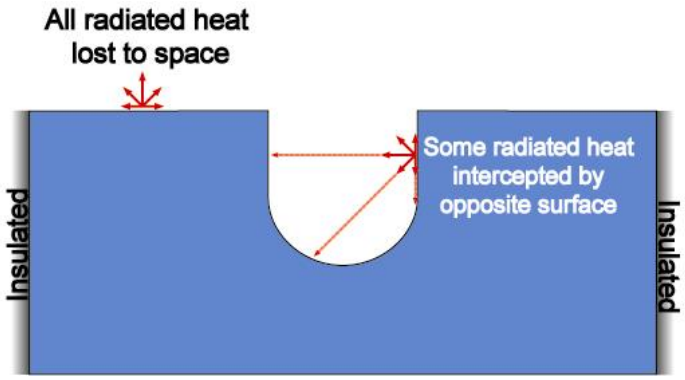


Figure 9. Schematic representation of radiation heat loss in the tile

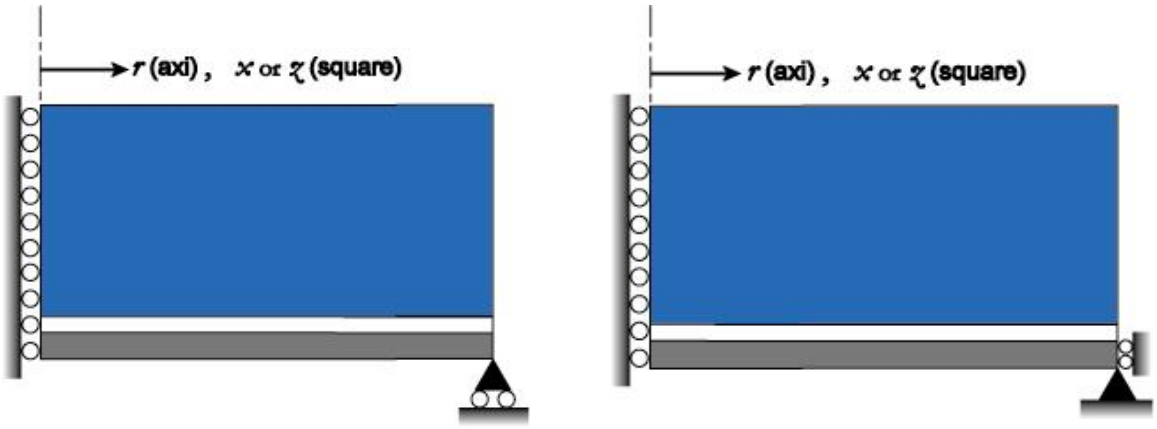


(a) unrestrained boundary condition, BC1 (b) restrained boundary condition, BC2

Figure 10. Structural boundary conditions applied to underlying structure

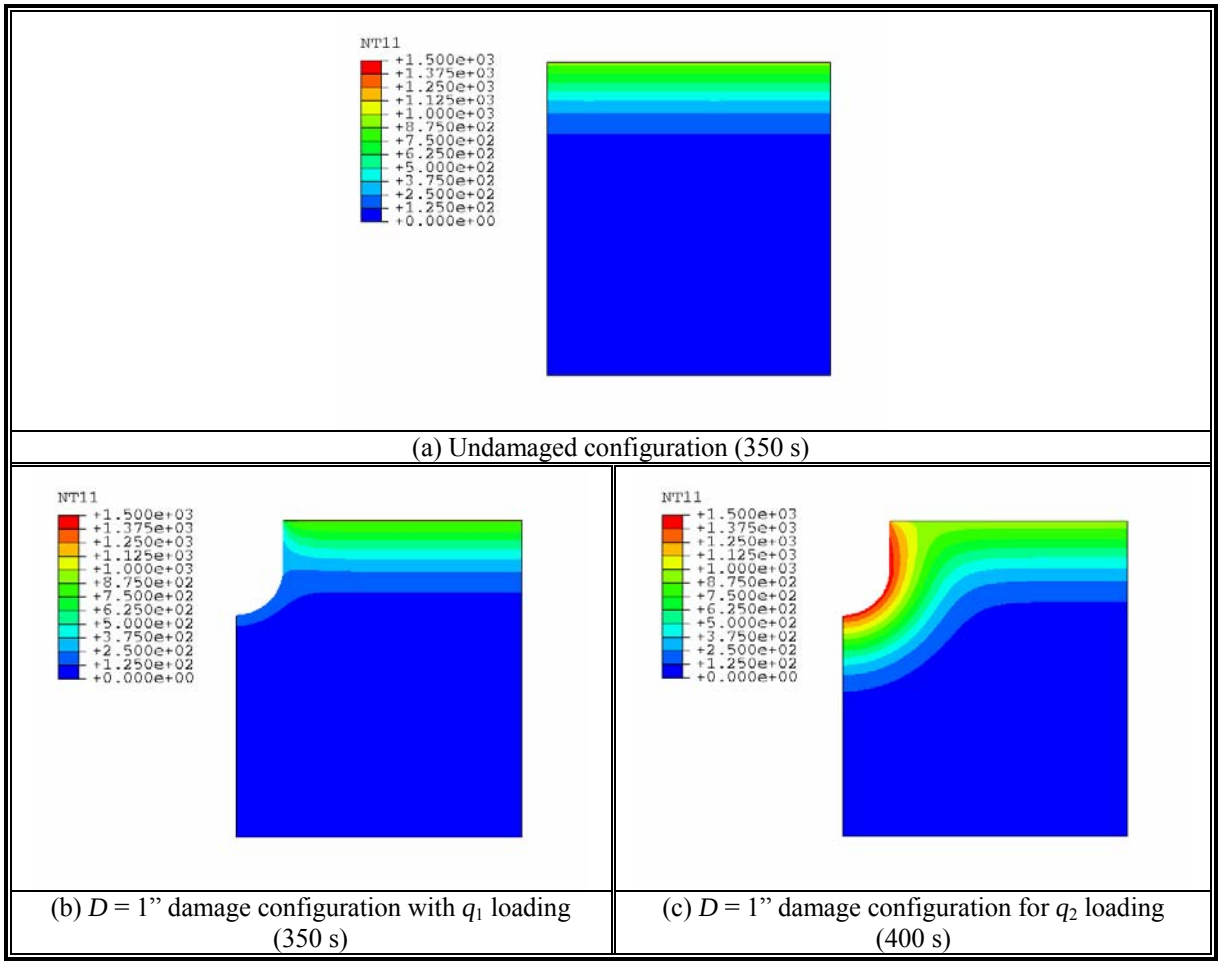


(a) Undamaged configuration (350 s)

(b) $D$ = 1” damage configuration with $q_1$ loading (350 s)

(c) $D$ = 1” damage configuration for $q_2$ loading (400 s)

Figure 11. Temperature contour plots for the undamaged and $D$ = 1" damaged axisymmetric configurations for the two different heat loads at times when the maximum von Mises stress in tile occurs. Legend indicates temperatures in °C.

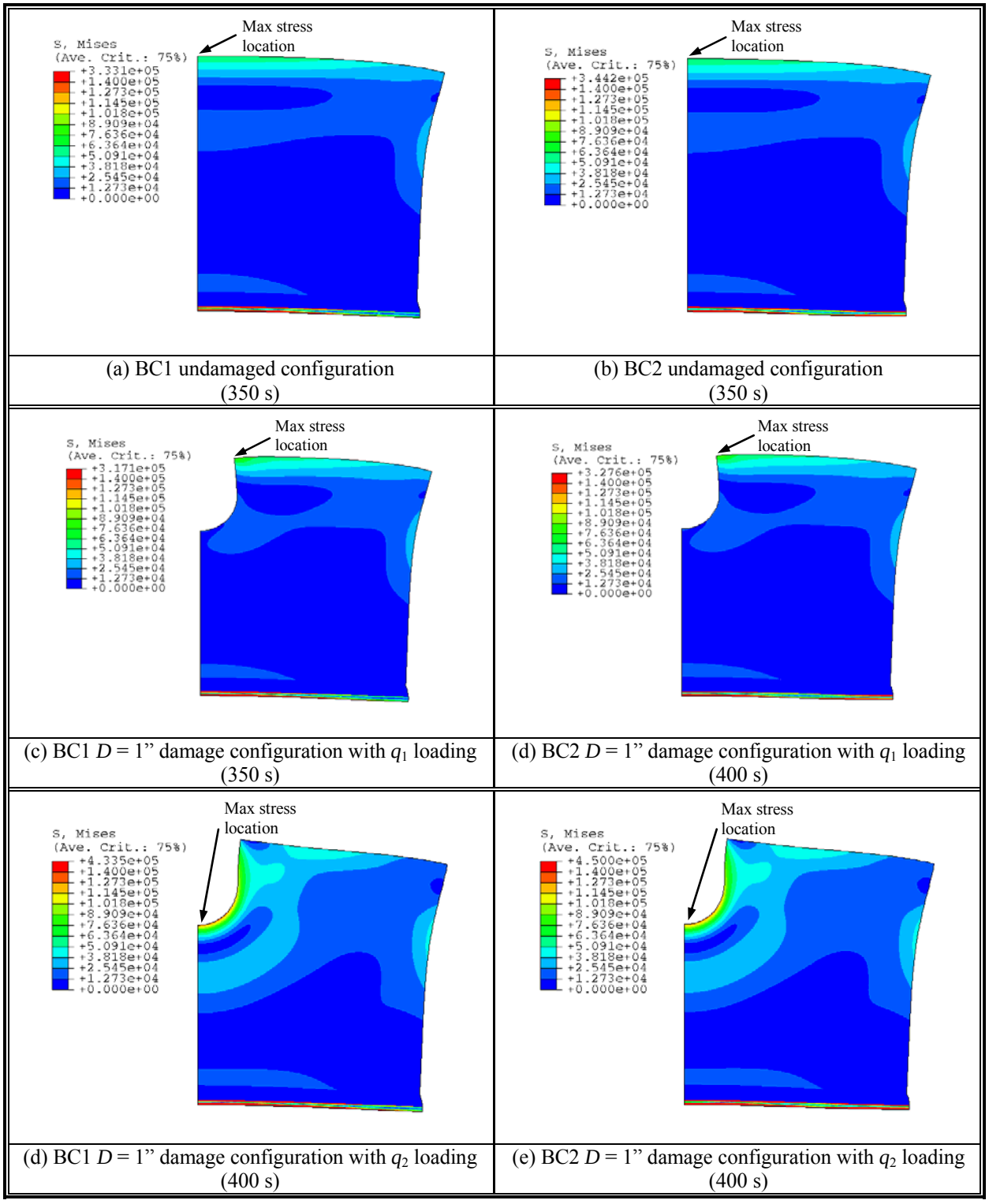


Figure 12. von Mises stress contour plots for the undamaged and $D$ = 1" damaged axisymmetric configurations for the two different heat loads at times when the maximum von Mises stress in tile occurs. Legends indicate stresses in Pascal.

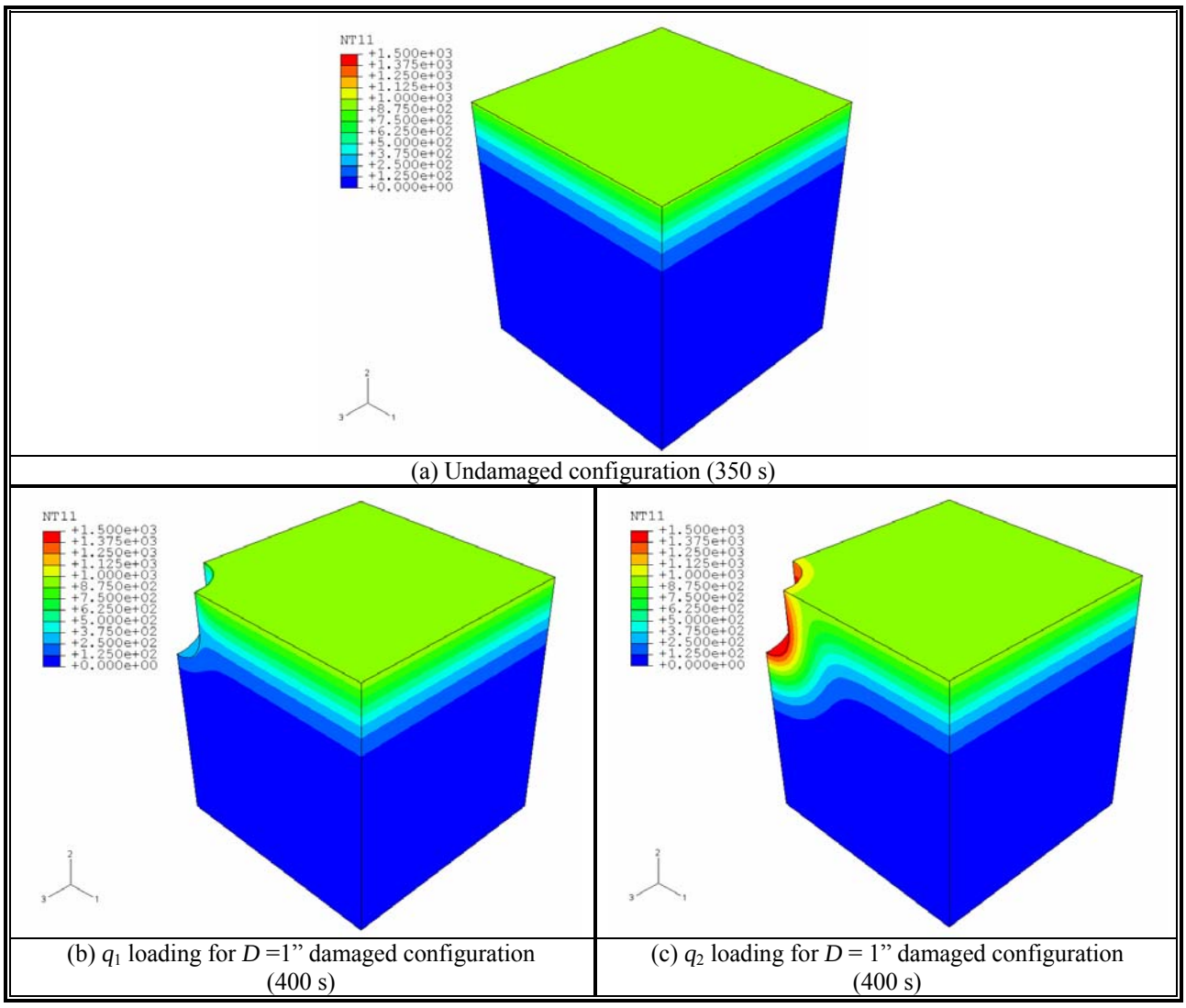


(a) Undamaged configuration (350 s)

(b) $q_1$ loading for $D$ =1" damaged configuration (400 s)

(c) $q_2$ loading for $D$ = 1" damaged configuration (400 s)

Figure 13. Temperature contour plots for the undamaged and damaged ($D$ = 1") square configurations for the two different heat loads at times when the maximum von Mises stress in tile occurs. Legends indicate temperatures in °C.

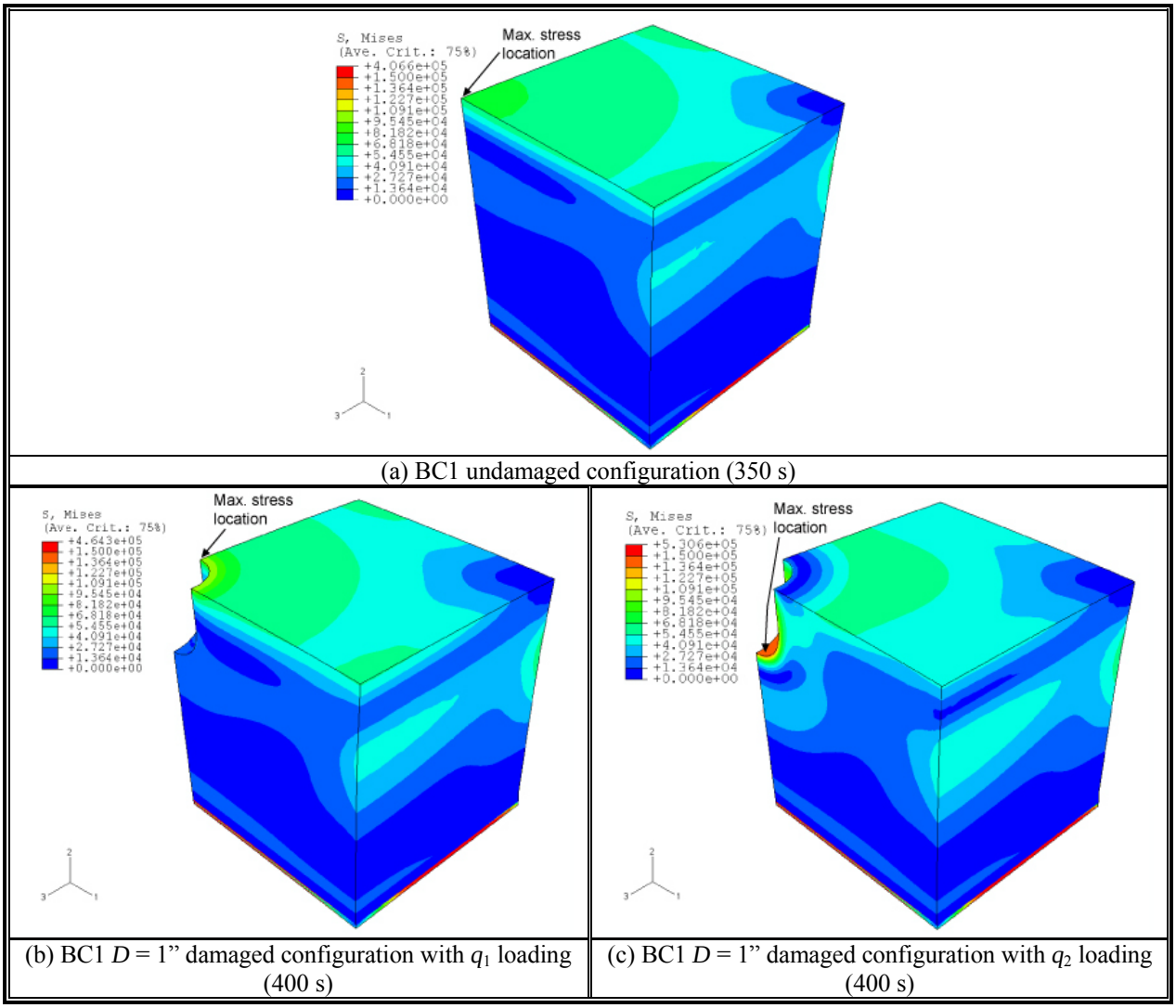


(a) BC1 undamaged configuration (350 s)

(b) BC1 $D$ = 1" damaged configuration with $q_1$ loading (400 s)

(c) BC1 $D$ = 1" damaged configuration with $q_2$ loading (400 s)

Figure 14. von Mises stress contour plots for the undamaged and D = 1" damaged square configurations for the two different heat loads at times when the maximum von Mises stress in tile occurs. Legends indicate stresses in Pascal

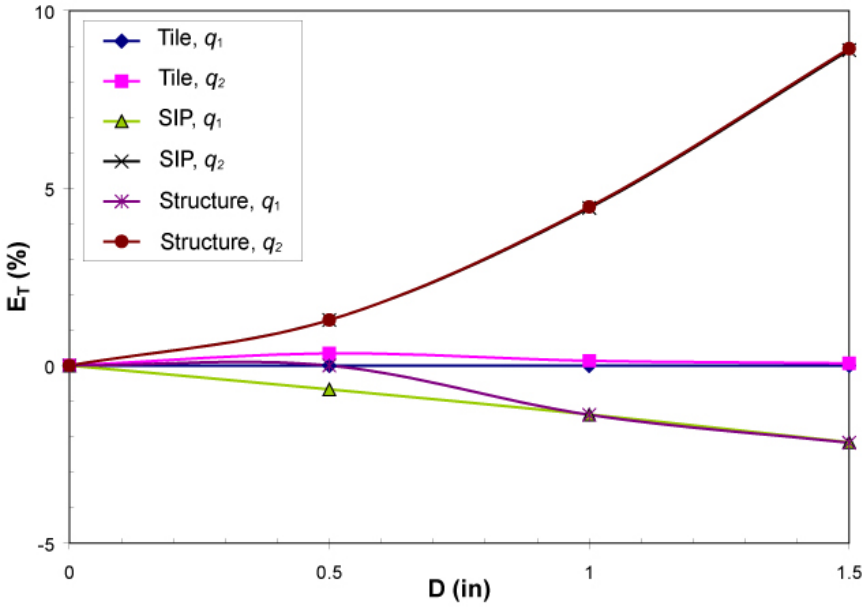


Figure 15. Comparison of maximum temperatures for axisymmetric and square configurations

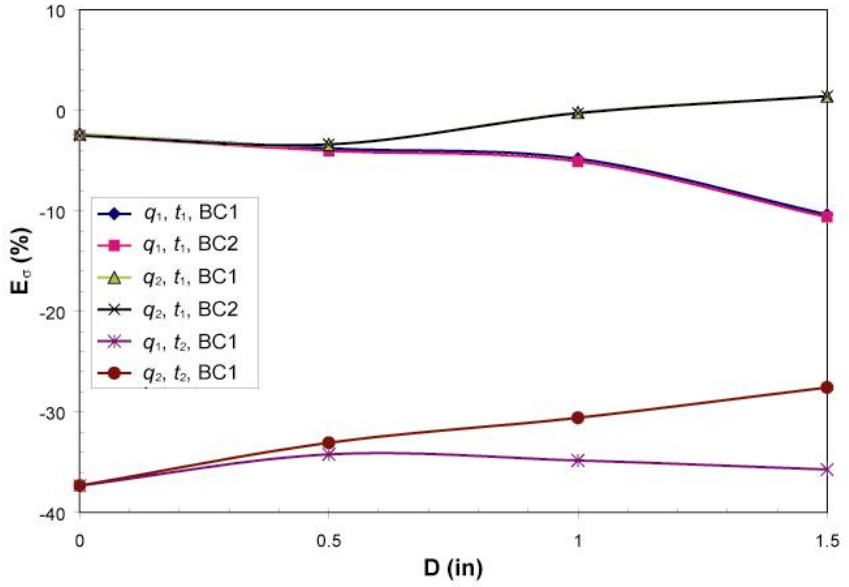


Figure 16. Comparison of maximum von Mises stresses in the tile for axisymmetric and square configurations

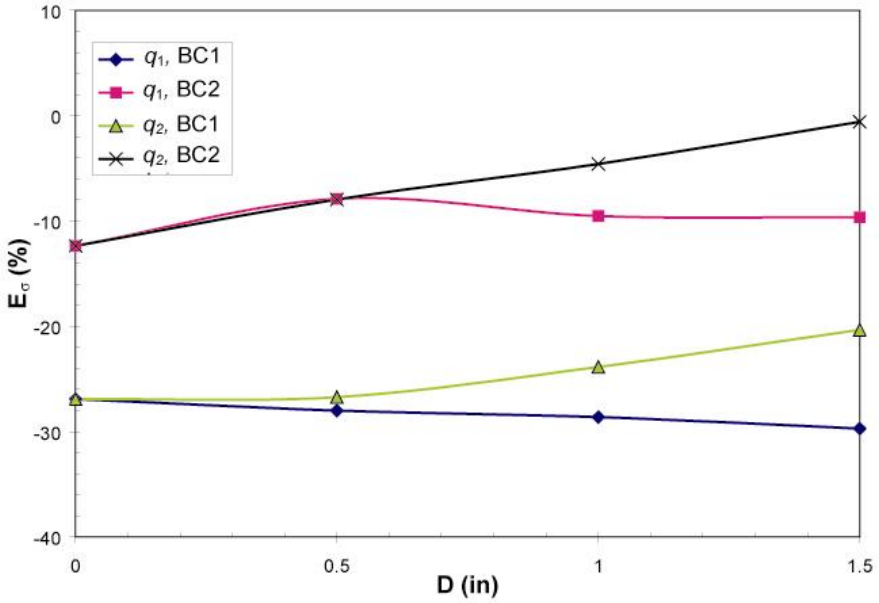


Figure 17. Comparison of maximum von Mises stresses in the SIP for axisymmetric and square configurations

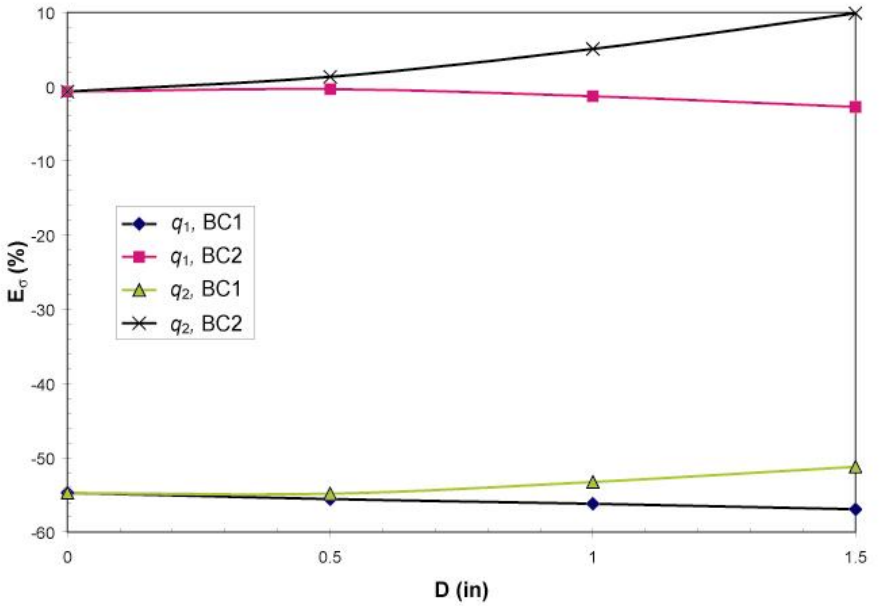


Figure 18. Comparison of maximum von Mises stresses in underlying structure for axisymmetric and square configurations